Tuning membrane properties to control supersaturation of antisolvent crystallization

Sara Chergaoui[1,2], Jimmy Lauzer[1,2], Damien P. Debecker[2,3], Tom Leyssens[2,3], Patricia Luis[1,2]

[1] Institute of Mechanics, Materials and Civil Engineering - Materials & Process Engineering (iMMC-IMAP), UCLouvain, Place Sainte Barbe 2, 1348 Louvain-la-Neuve, Belgium
[2] Research & Innovation Centre for Process Engineering (ReCIPE), UCLouvain, Place Sainte Barbe 2, 1348 Louvain-la-Neuve, Belgium
[3] Institute of Condensed Matter and Nanosciences (IMCN), UCLouvain, Place Louis Pasteur 1, 1348 Louvain-la-Neuve, Belgium

Abstract

The crystal morphology influences the properties of organic compounds, especially in pharmaceutics such as the dissolution and absorption of drugs in the human cells. In antisolvent crystallization, the crystal size and shape are tied to the degree of mixing and dosage of antisolvent, which could be controlled using membranes with specific morphology/surface properties. Little is known though on the relationship between membrane characteristics, antisolvent mass transfer and crystal properties. Flat sheet polyvinylidene fluoride (PVDF) membranes were prepared using non-solvent induced phase separation, to illustrate the impact of membrane characteristics on the resulting crystal size distribution (CSD) obtained using membrane-assisted antisolvent crystallization (MAAC). The crystallization of glycine was taken as case study. We showed the antisolvent transmembrane flux increased when the membrane thickness decreased, or when the hydrophobicity or the porosity increased. After MAAC operation, membranes had no significant change in surface functional groups, hydrophobicity nor structure. The best-performing membrane was found to have 119° hydrophobicity, 89.4% porosity and 140 µm thickness, reaching high reproducibility of CSD corresponding to stable transmembrane fluxes throughout 180 minutes of operation. The capacity of MAAC to consistently produce a narrow CSD at optimum membrane characteristics makes this technology very competitive with conventional crystallization processes.

Keywords: antisolvent membrane-assisted crystallization; organic compounds; transmembrane mass transfer; crystal size distribution

Graphical abstract

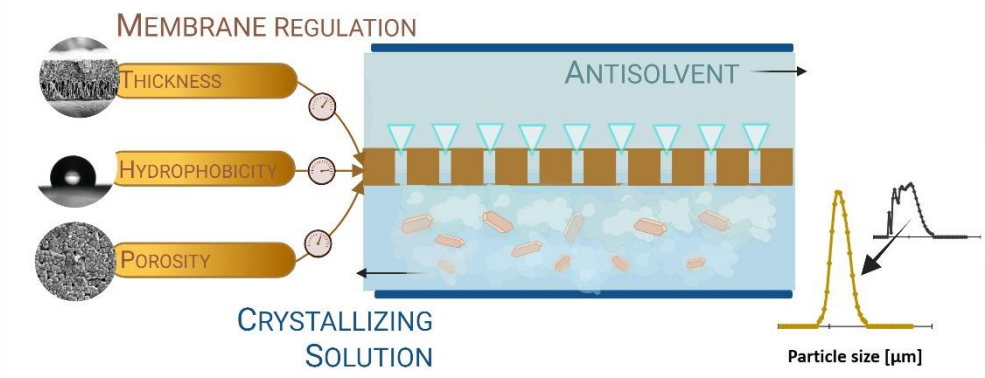

1. Introduction

The chemical and pharmaceutical industries are facing significant challenges regarding energy consumption and process intensification [1,2]. Membranes flourished as a technology that meets the sustainability goals, touching many areas like water purification [3–7], development of artificial organs [8,9], gas separation [10,11], carbon capture and conversion [12,13], distillation-crystallization [14–17], etc. This technology is at the verge of transforming the traditional antisolvent crystallization into a more compact and efficient process [18,20].

Antisolvent crystallization is frequently applied for the production of fine chemicals, pharmaceuticals, agrochemicals, and cosmetics [21], as these compounds are frequently sensitive to temperature variation, requiring the use of an antisolvent to reduce solubility [22]. Conventionally, antisolvent crystallization has been performed in stirred vessels which produces a wide crystal size distribution (CSD) [23]. The control of crystal size or CSD has been attributed to the control of mixing and dosage of the antisolvent [24], or the number entry points of the antisolvent in the system [25].

One approach adopted to obtain a uniform crystal size is to incorporate an impinging jet mixer in a crystallizing reactor, consisting of two jet nozzles arranged diametrically opposite where the antisolvent and crystallizing solution meet [26]. This impingement point is of high supersaturation causing a non-uniform nucleation [27]. Irregular mixing of the antisolvent and crystallizing solutions, and jet alignment are both limiting factors of this technique [28]. Another approach is the use of microchannels, which consist of the flow of liquids in devices of a few millimeters to micrometers [29]. This approach necessitates microchannels of meticulous dimensions that is costly and time-consuming. Empirically, the correlation between the operating conditions, the geometries of the microchannels and the particle size distribution has been difficult to obtain; on top, this technique faces scale-up difficulties [30]. The lack of uniform distribution of supersaturation points in a crystallizer jeopardizes the formation of a uniform crystal size and habit [31–33]. This can be mitigated with membrane-based technologies offering intense mixing and a controlled mass transfer of antisolvent.

In a membrane crystallizer, the membrane is not a mere selective barrier, it plays the role of a contactor between two liquid streams: the crystallizing solution and the antisolvent [34]. The activity gradient between the crystallizing solution side and the antisolvent's drives the permeation of the antisolvent through the membrane pores, increasing gradually the crystallization system's supersaturation with time (Fig. 1). The large contact between the solution and membrane surface results in a mixing adequate to produce crystals with uniform shape and size. This membrane-based technique, also known as membrane-assisted antisolvent crystallization (MAAC) is indeed able to generate a supersaturated environment in which crystals nucleate and grow with equivalent kinetics and

thermodynamics [35]. The polymeric surface also promotes heterogeneous nucleation, reducing the energy barrier necessary for nucleation and the induction time of the crystallization process [34].

The mass transfer of the antisolvent can be controlled either with the variation of the operating conditions or the membrane properties. Chen *et al.*, studied the mixing pattern at the shell side of hollow-fiber membranes using Computational Fluid Dynamics (CFD), predicting the optimum flow conditions [36]. Other empirical-based studies demonstrated that having the antisolvent flowing slightly faster than the crystallizing solution is necessary to avoid a reverse transmembrane flux [37–41], or insuring a temperature difference [42]. Chergaoui *et al.*, further investigated the impact of gravity, the antisolvent composition, flow rate and temperature on MAAC performance, using polypropylene flat sheet membranes. The optimized conditions gave a consistent crystal size distribution (CSD) with low coefficients of variation and different induction times [43]. As for membrane properties, depending on the crystallization system, previous studies (Table A1) either used a hydrophilic membrane when water was the antisolvent [40], or a poorly hydrophilic to hydrophobic membranes with WCA in the range of

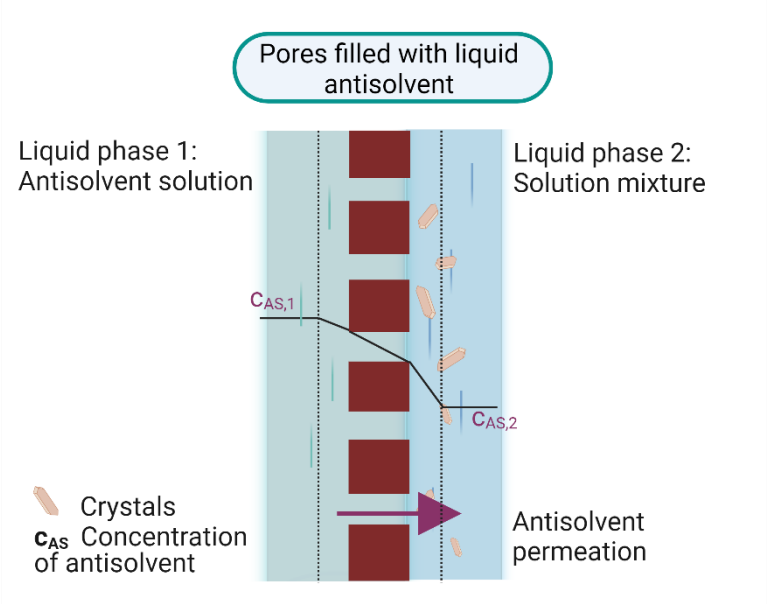

Fig. 1. Concentration profile of antisolvent through the membrane pores. A controlled mass transfer allows for a controlled supersaturation in the solution mixture.

83 to 150° when the antisolvent was organic such as ethanol or erythritol [38,43,44]. Meng *et al.*, found that superhydrophobic membranes resulted in a lower rate of solute deposition, and these solutes could be removed easier compared with the less hydrophobic membranes. Besides, either membrane gave a consistent crystal nucleation and growth [15]. Finally, Fern *et al.*, demonstrated that a lower membrane pore size resulted in a smaller mean crystal size due to the higher micro-mixing induced with a smaller pore size [39].

There exist several other studies that used either MAAC or a similar configuration, as a tool to meet specific crystallization objectives such as controlling polymorphism or producing co-crystals. In controlling polymorphism, Di Profio *et al.*, used polypropylene hollow fiber membranes to control the dosage of antisolvent from the ethanol/ water mixture to the crystallizing solution of L-Histidine in bi-distilled water. The latter crystallizes in two forms orthorhombic or monoclinic, depending on the antisolvent fraction in the solution which directly impacts the nucleation and growth rates [42]. The dosage of antisolvent into the crystallizing solution took place in this case thanks to the temperature difference to ensure a permeation of the antisolvent in the vapor phase. Likewise, using the temperature difference as a driving force, Caridi *et al.*, could control the mass transfer of the solvent to operate under

set conditions for co-crystallization [45,46]. In this work, the antisolvent permeates through the membrane in a liquid phase and uses the activity gradient as the driving force.

In this study, we explored the influence of key membrane characteristics, namely thickness, hydrophobicity, and porosity, on antisolvent crystallization. A mere comparison of the previous studies (see Table A1) falls short of achieving this goal for three reasons: (i) the difference of thermodynamic and kinetic conditions inherent in each crystallization system, (ii) insufficient information on membrane properties and (iii) on the resulting mass transfer and crystallization aspects such as CSD and supersaturation. Our aim is to clarify the exclusive role of the membrane in crystallization control by manipulating membrane properties through the non-solvent induced phase separation technique while maintaining the operating conditions such as the flow rate of antisolvent and crystallizing solutions, the temperature, and pressure in all experimental. Glycine-water-ethanol was used as the model crystallization system. Any crystallization model could have fit in this study under the condition of respecting the thermodynamics of the chosen system, as the objective here is to detect the correlation between the membrane properties and the resulting crystals, not to alter glycine properties. Finally, the membrane reusability and potential risks in performing MAAC were assessed. The subsequent findings support the development of MAAC as a technology able to strongly compete with conventional crystallization processes.

2. Materials and methods

2.1. Materials

The crystallizing solution was prepared by dissolving glycine from Sigma-Aldrich, Belgium, at a saturation concentration of 23 wt.%. A series of membranes were developed using non-solvent induced phase inversion. Polyvinylidene fluoride (PVDF) and polyvinyl chloride (PVC) were obtained from Sigma Aldrich (Belgium), and the solvents dimethylacetamide (DMAc), N-methyl-2-pyrrolidone (NMP), and dimethylformamide (DMF) were purchased from VWR (Belgium). The complete list of chemicals used in this work is included in Table 1. All the polymers were dried at 343 K overnight before use.

Table 1 List of chemicals used in this study.

Chemical	Supplier (Belgium)	Characteristics	Product code
Ultrapure Water	Lab	18.2 MΩcm	-
Glycine	Sigma-Aldrich	**Purity:** ≥99.5%	56-40-6
FMOC Chloride	Sigma-Aldrich	**Purity:** ≥99.0 %	28920-43-6
Acetonitrile	VWR Chemicals	**Purity:** ≥99.95 %	75-05-8
Methanol	VWR Chemicals	**Purity:** ≥99.8 %	67-56-1
Norvaline	Sigma-Aldrich	**Purity:** ≥99.0 %	760-78-1
Polyvinylidene fluoride	Sigma-Aldrich	**MW:** 180000	24937-79-9
Polyvinyl chloride	Sigma-Aldrich	**MW:** 43000	9002-86-2
N-dimethylformamide	VWR Chemicals	**Purity:** ≥99.9%	68-12-2
N-methyl-2-pyrrolidone	Acros Organics	**Purity:** 99%	872-50-4
Tetrahydrofuran	VWR Chemicals	**Purity:** ≥99.0 %	109-99-9
N,N-Dimethylacetamide	Alfa Aesar	**Purity:** 99%	127-19-5
3-Mercaptopropionic acid	Sigma-Aldrich	**Purity:** ≥99.0 %	107-96-0
Ethanol absolute	VWR Chemicals	**Purity:** ≥99.5%	64-17-5
Orthophosphoric acid 85%	VWR Chemicals	**Purity:** 85.6 %	7664-38-2
Phthaldialdehyde	Sigma-Aldrich	**Purity:** ≥99.0 %	643-79-8

2.2. Membrane synthesis and characterization

2.2.1. Membrane synthesis

The aim of this study is to understand the correlation between key membrane properties and the resulting crystal characteristics, plus shed light on any limitations that face membranes for MAAC applications. This objective is attained by developing membranes of different characteristics in terms of thickness, hydrophobicity, and porosity. The variation of membrane thickness consisted of varying the height of the casting knife while using a dope solution composition of PVDF polymer at 22 wt% and a mixture of solvents THF and NMP [47]. Membrane hydrophobicity was varied using a polymer blend of PVDF and PVC with NMP solvent [48]. Finally, the porosity varied according to the solvent used in dope solution as it results in different dope solution viscosity hence impacting the dissolution rate. Table 2 summarizes the solution compositions for each set of membranes.

All solutions were stirred overnight under a temperature of 343 K, then kept 24 hours for degassing before casting. As for membrane casting, the Elcometer 4340 Automatic Film Applicator was used at room temperature (20 °C) with a casting knife set at various thicknesses from 150 to 250 µm. After casting, the membrane was directly submerged in a demineralized water bath for phase separation. The formed membranes were kept in the water bath for 24 hours for a complete phase separation before evaluation in MAAC.

Table 2 Composition of dope solutions utilized for the development of membranes of various thicknesses, hydrophobicity and porosities.

Objective	**Polymer**	**Concentration** ***wt. %***			**Solvent**	**Concentration** ***wt. %***	**Casting thickness** ***µm***		
Variation of membrane thickness	PVDF	22			THF	7.8	**{M₁}** 150	**{M₂}** 200	**{M₃}** 250
					NMP	70.2			
Variation of membrane hydrophobicity		**{M₄}**	**{M₅}**	**{M₆}**	DMF	78	200		
	PVDF	15.4	17.6	19.8					
	PVC	6.6	4.4	2.2					
Variation of membrane porosity	PVDF	22			**{M₇}** DMF	78	200		
					{M₈} NMP				
					{M₉} DMAc				

2.2.2. Membrane morphology

The morphology of membranes developed in this study was assessed using Scanning Electron Microscope (SEM) (Zeiss, ULTRA). A clean cross-section was obtained by immersing the membrane sample in liquid nitrogen. Prior to SEM imaging, samples were made conductive with the deposition of a thin gold layer using a sputter coater (Balzers Union FL 9460 BALZERS SCD 030).

2.2.3. Membrane hydrophobicity

Optical Contact Angle (OCA) DataPhysics OCA20 was employed to measure the water contact angle (WCA) at the membrane surface taking three measurements into account for each membrane sample. The sessile drop method with a 5 µL droplet of water was followed.

2.2.4. Membrane porosity and thickness

The membrane thickness was measured using a micrometer at three measurement points of the membrane sample. As for the membrane porosity, the Archimedes method was employed such that, for

each membrane sample, three mass values were recorded:

- Immersed sample in the solvent (pure ethanol);
- Wet sample mass: the membrane samples were immersed for 24 hrs in pure ethanol prior to air measurement;
- Dry sample: membranes were dried for 2 hrs under 100 °C to avoid presence of water.

These values enabled the calculation of sample density, and eventually the porosity value as in:

$$\varepsilon = \frac{Volume_{void}}{Volume_{solid}}$$

Ethanol density used was 787.9 Kg/ m^3 corresponding to a temperature of 21.5 °C.

2.2.5. Membrane crystal entrapment

To evaluate the presence of any crystals entrapped in the membrane after MAAC operation, the thermogravimetric (TGA) analysis was used to quantitively compare between pristine membranes and the used ones. TGA/SDTA 851^e of Mettler Toledo analyzed all membrane samples from 30 to 600°C at a heating rate of 10K/min under N_2 atmosphere (50 ml/min).

2.2.6. Membrane surface characteristics

Thermo Scientific Nicolet iN10 was used to perform Fourier-transform infrared spectroscopy (FTIR) in the range 4000 and 400 cm^{-1}. Functional groups at the membrane surface allowed us to verify any membrane surface modification after MAAC operation.

2.3. Membrane performance in MAAC and mass transfer

The evaluation of membrane performance in MAAC was conducted using an in-house set-up (Fig. 2 and S1). The membrane module with an effective membrane dimension of 12×10 cm, was purchased from DeltaE Srl, Italy. Glycine was dissolved in ultrapure water at room temperature (23-25 °C) and a concentration of 23 wt %. This solution represented the model crystallizing solution which was circulated by a gear pump through the lower membrane cell at 3.3 $\times 10^{-4}$ $m.s^{-1}$ (ColeParmer, Belgium). Pure ethanol was used as antisolvent solution and was circulated through the membrane module upper cell using the gear pump Verder, Belgium, at 5 $\times 10^{-4}$ $m.s^{-1}$. The turbidity meter was used to accurately detect the induction times, while the balance recorded the mass of the antisolvent solution as it permeated over time through the membrane.

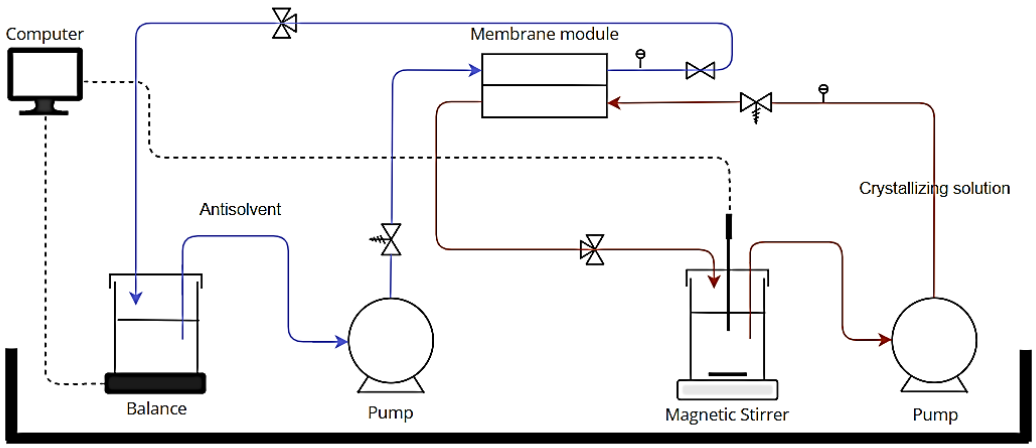

Fig. 2. A schematic representation of the setup developed to assess membrane performance.

198 *2.3.1. Antisolvent transmembrane flux:*

199 The mass of the antisolvent compartment was recorded over time to verify the mass transfer through
200 the membrane in terms of net flux (Equation1) and mass transfer coefficient (Equation 2). The product
201 of the mass in the crystallizing solution compartment and the weight fraction of ethanol given by gas
202 chromatography constituted the net mass of ethanol in the solution over time:

203 $$J = \frac{1}{A}\frac{w_{as}(t_{i+1}) - w_{as}(t_i)}{t_{i+1} - t_i} \quad \text{(Eq. 1)}$$

204 With J the net transmembrane flux of ethanol (antisolvent) in kg/m^2.s, A the effective area of the
205 membrane (0.012 m^2), t_i the operation time i in s, and w_{as} the weight of the antisolvent in kg.

206 The mass transfer coefficient was deduced from the relationship between the transmembrane flux and
207 the activity of ethanol in solution:

208 $$J = K.\frac{\left(a_f(t_{i+1}) - a_{as}(t_{i+1})\right) - \left(a_f(t_i) - a_{as}(t_i)\right)}{\ln\left(\frac{\left(a_f(t_{i+1}) - a_{as}(t_{i+1})\right)}{\left(a_f(t_i) - a_{as}(t_i)\right)}\right)} \quad \text{(Eq. 2)}$$

209 With K, the overall mass transfer coefficient in kg/m^2.s; a_f and a_{as} are the ethanol activities at the feed
210 and the antisolvent sides respectively. The activity accounts for the non-ideality of the solution such
211 that $a = x.\Upsilon$, x being the ethanol weight fraction in the solution mixture and Υ the activity coefficient.
212 The activity coefficient values were obtained using the UNIFAC estimation of water/ethanol binary
213 interactions at incremental mass fraction of ethanol from 0 to 1, modelled in ASPEN Plus V11 (Fig.
214 S2).

215

216 *2.3.2. Supersaturation:*

217 The ratio between the solute concentration (c_i) in the crystallization solution and its concentration
218 at equilibrium under same temperature (c*) was used to express the supersaturation of glycine [49].
219 The index i stands for the time the measurement was taken:

220 $$S = c_i/c^*$$

221 *2.3.3. High Pressure Liquid Chromatography (HPLC):*

222 Glycine concentration was quantified both in the antisolvent and the crystallizing solution. Glycine
223 content in the antisolvent verifies for any counter transfer of crystallizing solution through membrane,
224 while the concentration of glycine in the crystallizing solution was used to compute supersaturation. A
225 Shim-pack GIST C18 column from Shimadzu, Belgium, was used to enable glycine distinction from
226 the sample mixture. Samples were composed of 1:1 solution of the sample retrieved from experimental
227 after dilution, plus the standard 4mM Norvaline solution. Samples retrieved from crystallizing solution
228 were diluted by a factor of 1600 with ultrapure water and a factor of 400 for solutions retrieved from
229 the antisolvent solution. Small traces to no glycine is expected to have dissipated to the antisolvent
230 compartment. The calibration curve is described in Fig. S3.

231 *2.3.4. Gas Chromatography (GC):*

232 The concentration of the antisolvent, ethanol, was measured thanks to the gas chromatograph
233 Thermo Scientific™ - TRACE 1300 equipped with a flame ionization detector (FID). On one hand, the
234 concentration was tracked in the antisolvent solution side to verify for any drop of concentration that
235 could have been induced with the reverse flux by the crystallizing solution. On the other hand, the
236 concentration of antisolvent in the crystallizing solution was used to deduce the supersaturation level.

Sample preparation for analysis comprised a 1:1 mixture of the mother solution and a 0.01 wt.% acetonitrile solution. The calibration curve used for final data is given in Fig. S4.

2.4. Crystal properties

2.4.1. Solubility

Water and ethanol mixtures were prepared using ethanol concentrations of 0, 20, 40, 60, 80, and 100 wt. % along with an excess of glycine. These mixtures were stirred at a temperature of 20°C for a duration of 12 hours before being filtered using a vacuum. The filtrate was then dried for a total of 72 hours, during which its weight was recorded at 24-hour intervals. The recorded weight changes were indicative of the quantity of glycine that had dissolved in the solution. This data was utilized to construct the solubility curve as illustrated in Fig. S5.

2.4.2. Crystal shape

Crystals were retrieved from both the surface of the membrane and the overall crystallizing solution after each experiment. Subsequently, they were allowed to dry in a fume hood overnight. For conductivity, a thin layer of gold was applied using a sputter coater (BALZERS UNION FL 9460 BALZERS SCD 030) under a vacuum onto the samples.

2.4.3. Crystalline form

To analyze the crystalline structure of glycine crystals, powdered samples were examined using X-ray diffraction (XRD) within the range of 10 to 100 degrees (2theta). The XRD analysis was performed using a Bruker D8 Advance instrument with Cu Kα radiation at a wavelength of 1.5406 Å.

2.4.4. Crystal size distribution

Particle size distribution analysis was conducted using the SYNC particle analyzer, that analyses materials across a broad size spectrum ranging from 0.01 to 4000 micrometers. This analysis was based on static light scattering principles. For glycine, a refractive index of 1.4264 was established. The outcome presented by the SYNC 5000 instrument represent the average derived from three separate measurements carried out for data acquisition in this study.

2.4.5. In-line turbidity measurement

An InPro 8200 turbidity meter from Mettler Toledo in Belgium was utilized to monitor the fluctuation in solution turbidity throughout the experimental runtime. The implementation of in-line measurement enabled the recording of turbidity evolution at one-second intervals, giving precise determination of the induction time.

3. Results and discussion

3.1. Membrane characteristics

PVDF is a polymer that is widely used in membrane crystallization (MCr) applications, available both commercially and custom-made in different module forms [50–53]. Porous membranes of incremental thicknesses of 70 (M_1), 100 (M_2) and 140 µm (M_3) were developped, while maintaining the same hydrophobicity with a water contact angle (WCA) of 106° (Fig. 3) and similar porosity of ca. 87% (Table 3). Differences in the membrane thickness were solely related to the casting thickness, which was varied between 150 and 250 µm. The remaining casting conditions such as the dope solution

composition, the non-solvent composition (deionized water), the exposure time before submerging in coagulation bath and drying time, were kept the same.

To investigate the impact of membrane hydrophobicity, three membranes were synthesized (M_4 to M_6) using PVDF/ PVC polymer blend resulting in variation of membrane water contact angle of 99, 108 and 119° while maintaining same thickness of 60 µm and a porosity of ca. 87 %. Membrane hydrophobicity was altered by varying the composition of PVC and PVDF polymer blend; the higher the concentration of PVC, the less hydrophobic the developed membrane is, given that PVC polymer is intrinsically less hydrophobic than PVDF [54].

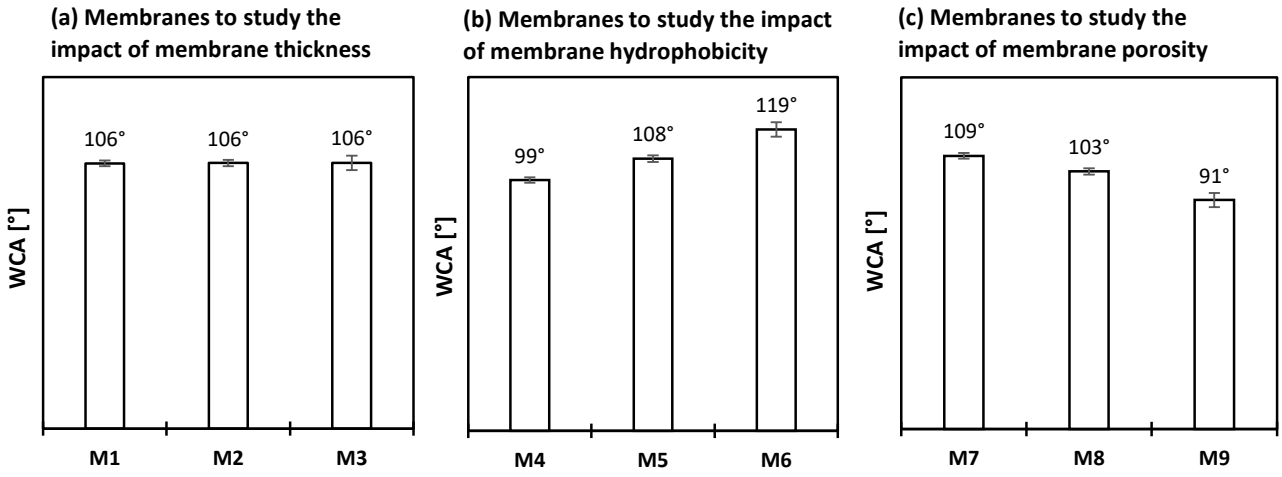

Fig. 3. Hydrophobicity of the 9 membranes developed using NIPS with variation of: (a) casting thickness, (b) PVDF/ PVC composition, and (c) solvent used to prepare dope solution.

Table 3 Characteristics of membranes developed using NIPS varying casting thickness and dope solution composition to study the impact of membrane thickness (M_1-M_3), hydrophobicity (M_4-M_6), and porosity (M_7-M_9).

Membrane	M_1	M_2	M_3	M_4	M_5	M_6	M_7	M_8	M_9
Thickness [µm]	70 ± 0.83	100 ± 0.55	140 ± 0.32	60 ± 0.31	60 ± 0.84	60 ± 0.63	100 ± 0.64	101 ± 0.54	100 ± 0.32
Porosity [%]	89.3 ± 0.3	87.9 ± 0.1	88.5 ± 0.2	89.8 ± 0.2	88.6 ± 0.05	87.8 ± 0.3	83.9 ± 0.1	86.4 ± 0.08	89.4 ± 0.1

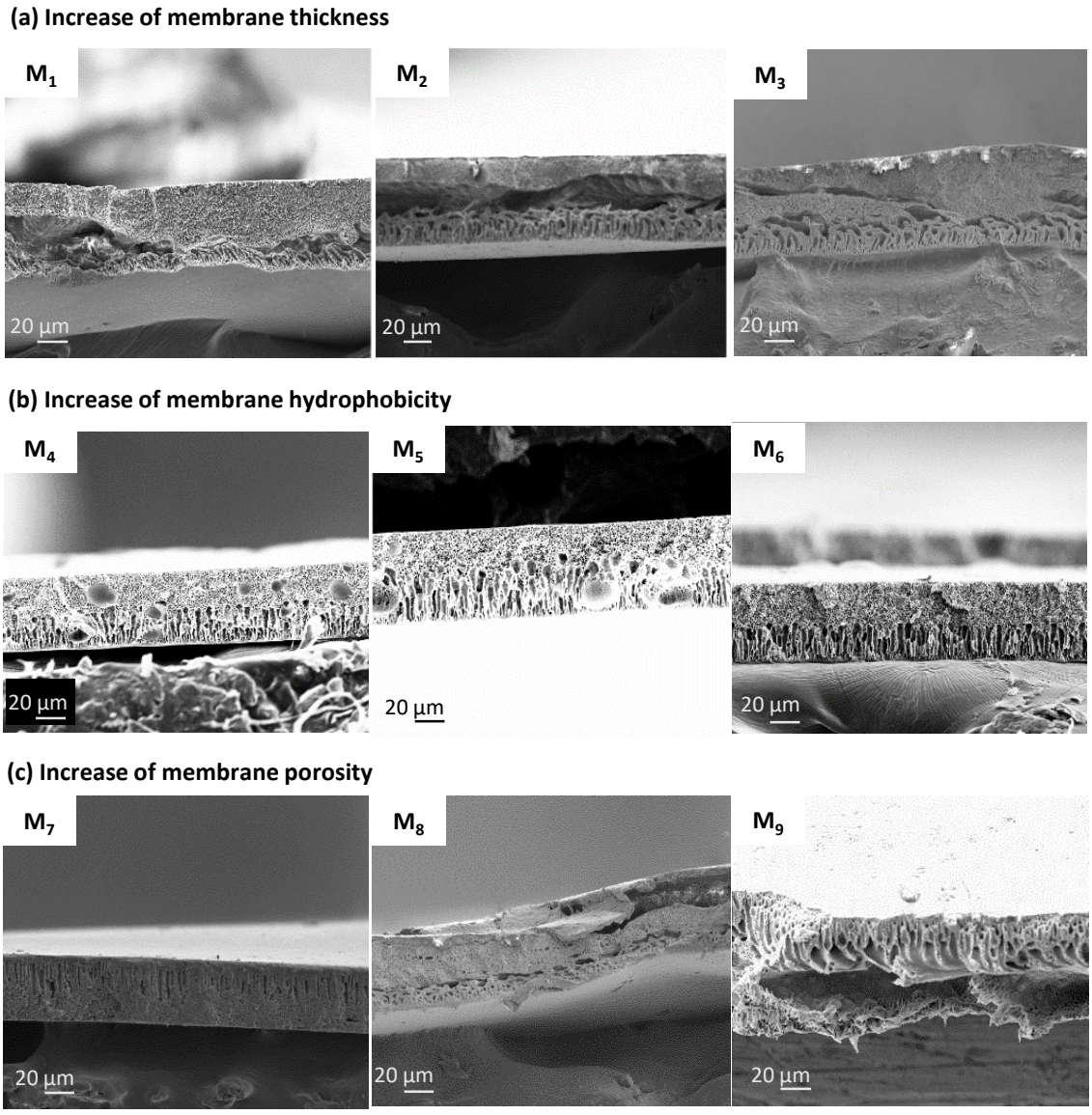

Fig. 4. Cross-sectional structure of membranes with incremental (a) thickness (b) hydrophobicity and (c) porosity. Membranes with highest to lowest value for either thickness, hydrophobicity of thickness are presented from top to bottom respectively.

Finally, the effect of membrane porosity was investigated at porosity values of 83.9, 86.4 and 89.4%, having a common thickness of 100 µm, and a WCA varying between 91 and 109°. The porosity of the membrane was mainly attributed to the density of voids that increased with intrusion rate of water into the casting film, which is a function of water miscibility in either NMP, DMAc or DMF solvents [55].

PVDF is a semi-crystalline polymer which undergoes precipitation when immersed, resulting from either liquid-liquid interactions or crystallization [56]. The cross section of these nine membranes comprised a mixture of finger-like and sponge-like structure (Fig. 4). This structure is closely tied to the kinetics and thermodynamics taking place between the solvent, polymer and non-solvent during the phase separation process [53,57]. The dope solution of membranes M_1-M_3 contained a ratio of 1:9 THF to NMP solvent mixture. Given that THF is more volatile and has weaker affinity with water, a first sponge-like layer is formed when the polymer film is immersed in water, which was responsible for delaying the completion of phase separation [58]. DMF on the other hand has stronger affinity to water, and led to a faster solvent/ non-solvent exchange rate, so the membranes M_4-M_6 had a thicker finger-

like sublayer. Besides, the presence of PVC polymer is responsible for the circular macro-voids formed more in M_4 and M_5 representing the voids between the PVDF and PVC crystals [54]. Finally, depending on the solvent power where DMAc>NMP>DMF [59], the membrane showed larger macrovoids from M_7 to M_9.

The hydrophobicity of the developed membranes was necessary to prevent the reverse flux by the crystallizing solution. It is also expected that membrane hydrophobicity will affect the transmembrane flux, responsible for induction time and final CSD. The range of membrane hydrophobicity (99 to 119°), thickness (70 to 140 µm), and porosity (83.9 to 89.4%) is consistent with the properties of reported in literature [50,52,60]. The porosity of the membrane was mainly attributed to the density of voids that increased with intrusion rate of water into the casting film, according to water miscibility in either NMP, DMAc or DMF solvents [55].

3.2. Effect of membrane properties on the mass transfer

Membrane thickness and porosity altered the transmembrane flux of the antisolvent as expected: the antisolvent transmembrane flux is higher with thinner membranes (Fig. 5a), and with higher porosity (Fig. 5c). The antisolvent faces less membrane resistance with the decrease of thickness or with the increase of the void volume in the membrane. Interestingly, an initial drop of transmembrane flux was not observed, compared to our previous study with the commercial polypropylene and polyvinylidene difluoride membranes [35], and observed as well by Tuo *et al.,* [35]. The main difference in this study is the asymmetry of pores dimensions, which may be the reason of higher flux stability over time. The pore shape was proven to play a role in promoting nucleation of Aspirin for example where Diao *et al.*, demonstrated that spherical nanopores hindered nucleation of Aspirin crystals, whereas angular nanopores of the same size promoted it. They propose that pore shape affects nucleation kinetics through the alteration of the orientational order of the crystallizing molecule near the angles of the pores [61].

Membranes M_4 and M_5 are more hydrophilic compared to M_6, which means they could be wetted easier with the crystallizing solution and according to the Classical Nucleation Theory (CNT), these surfaces promote more nucleation [62]. The mass transfer of ethanol was higher in M_4 and M_5 (Fig. 5b). This is attributed to first, the macro-voids between PVC and PVDF crystal interface that were observed previously in M_4 and M_5, offered slightly higher porosity to these membranes, reducing membrane resistance. Second, the affinity of ethanol towards the membrane matrix increases with lower hydrophobicity, leading to a faster transmembrane transfer of ethanol [63,64].

Overtime, the flux declines for all membranes, but this effect is more prominent for the 70 µm-thick membrane, followed by 100 and 140 µm-thick membranes. This can be explained by a higher antisolvent flux for these membranes, and a more rapid crystal formation. As these crystals in part have longer residence time at the vicinity of the membrane surface (not in the membrane pores), the resistance to the antisolvent mass transfer increases. The faster appearance of crystals is also expected to be promoted with the reduction of activation energy required for nucleation to occur over time.

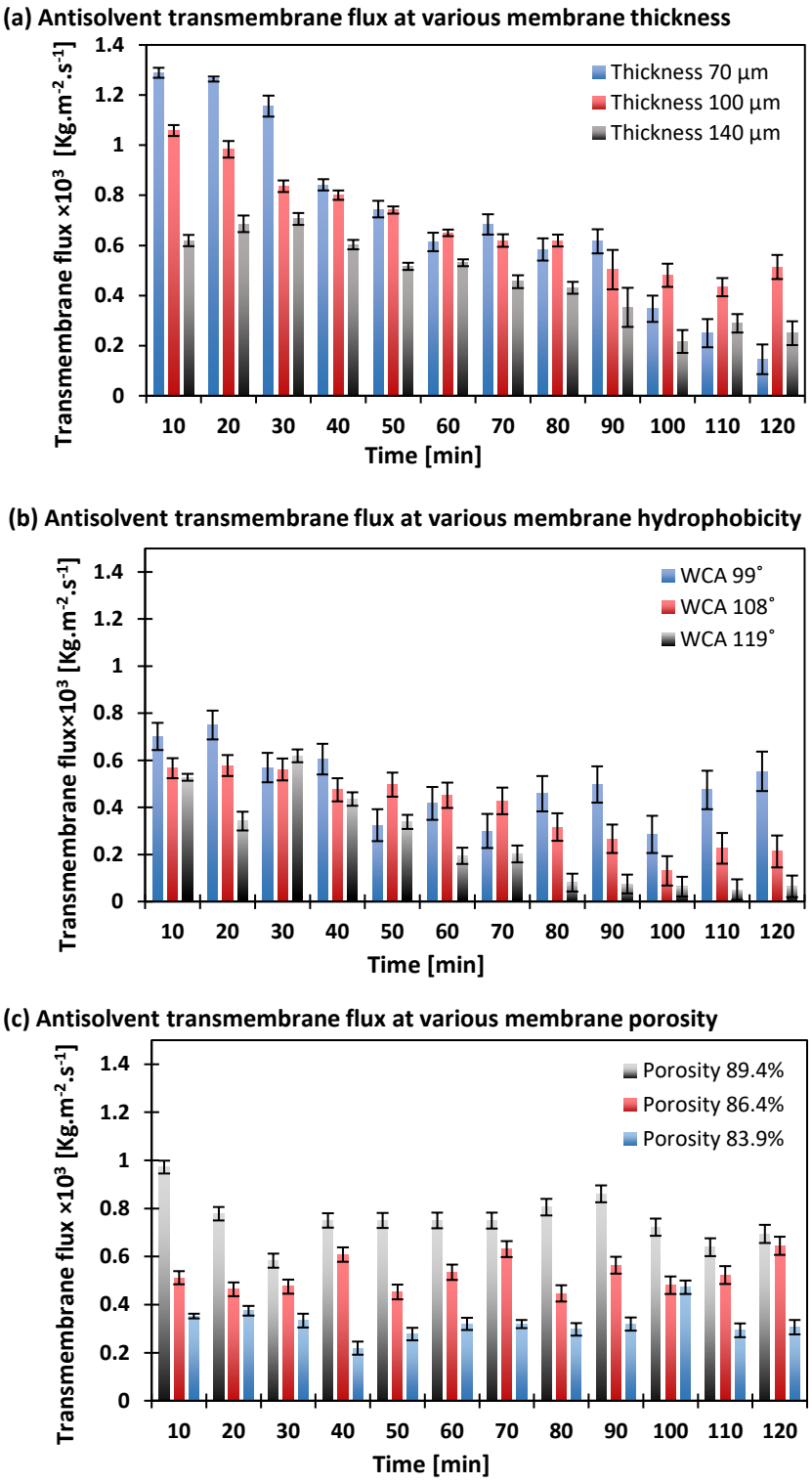

Fig. 5. Antisolvent transmembrane flux through membranes with incremental (a) thickness, (b) hydrophobicity and (c) porosity.

The transmembrane flux was evaluated considering the exact concentration of the antisolvent (ethanol) in both sides of the membrane with time. This allows for accurate representation of the transmembrane flux; besides, to allow for a sound comparison between membranes using other driving forces such as the temperature of pressure gradient, the mass transfer coefficient is deemed crucial to identify the impact of the membrane properties solely regardless of the driving force [65]. The mass

transfer coefficient followed the same trend as the transmembrane flux: the thiner, the less hydrophobic or the more porous the membrane, the higher the transmembrane mass transfer coefficient (Fig. 6). Small onset fluctuations of $\pm 0.05\times10^{-4}$ Kg.m^{-2}.s^{-1} of the mass transfer coefficient can be explained by the time required for the system to stabilize at the beginning. As for variation of the mass transfer over operation time, it is due to the variation of crystal growth and the membrane characteristics over time.

Porous membranes of various thickness, hydrophobicity or porosity have performed well in the sense that the mass transfer coefficient was stable throughout the operational time, while the flux varied according to the change in the driving force and the mixing conditions at the membrane surface. The reverse flux by the crystallizing solution to the antisolvent side is a limiting factor to the performance of MAAC, though. Thus, it was verified via the quantification of ethanol and glycine in the antisolvent solution. A slight decrease in the ethanol concentration was observed (Fig. S6) consistent with our previous study [35], but no traces of glycine were detected, indicating only water permeance. In this study, we understood that the reverse permeation of the crystallizing solution to the antisolvent side can be avoided either by keeping the flow rate of the antisolvent solution higher than the crystallizing one, and/ or having an asymmetric membrane structure with smaller pore sizes preferably at the crystallizing solution side given an adequate membrane hydrophobicity and thickness.

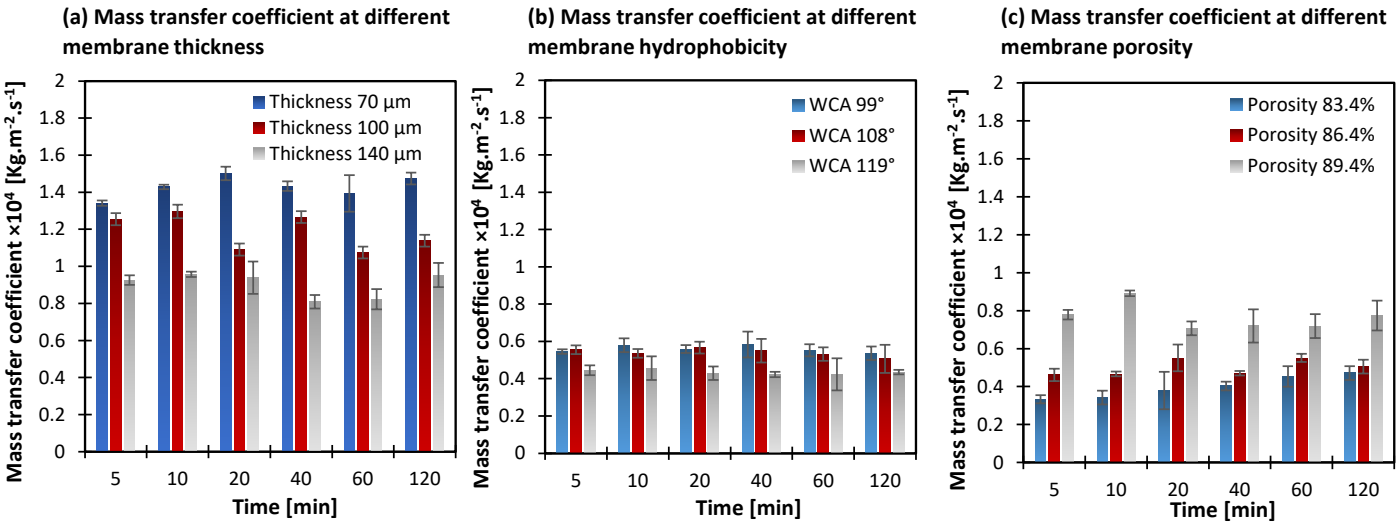

Fig. 6. Antisolvent mass transfer coefficient through membranes with incremental (a) thickness, (b) hydrophobicity and (c) porosity.

3.3. Effect of membrane properties on crystal size and morphology

3.3.1. Supersaturation

The increase of antisolvent in the crystallizing solution decreases the solubility of the solute and induced supersaturation (Fig. 7). The time required for the appearance of the first crystals in the crystallization solution, i.e., the induction time, was 58.4, 62.1 and 68.8 min for the membranes with thickness 70, 100 and 140 µm respectively. This induction time was 71.3, 78.2 and 91.7 min for membranes with water contact angles of 99, 107 and 119° respectively, and was 85.4, 66.4 and 51.1 min for membranes of 83.9, 86.4 and 89.4% porosity respectively (Fig. S8). This agrees with the supersaturation evolution, which exceeds S=1 during the time interval 50-100 min.

The antisolvent concentration in the crystallizing solution gives information on the crystallization yield. The final ethanol concentration ranged from 20 to 26 wt.%, while the maximum crystallization

yield can be achieved at ethanol concentration of ca. 60 wt. % from the solubility data (Fig. S5). Nonetheless, it is possible to further increase the crystallization yield with optimum membrane characteristics as will be discussed in Section 3.5.

Antisolvent addition rate plays a crucial role in dictating the nucleation point [66]. Supersaturation ratio varied the least under the membrane porosity factor. This agrees with the previous antisolvent transmembrane flux, which was least impacted by membrane porosity, so it is expected that the CSD would not vary significantly under variation of membrane porosity. In fact, a higher porosity correlated with a decrease in hydrophobicity, so the combination of hydrophobicity and surface porosity was responsible for the similarity in antisolvent transmembrane mass transfer. Most importantly, under all membrane conditions, it was observed that the supersaturation incremented smoothly solely due to the activity difference, without the need to exert additional heating or a pressure gradient as a driving force to the transmembrane mass transfer.

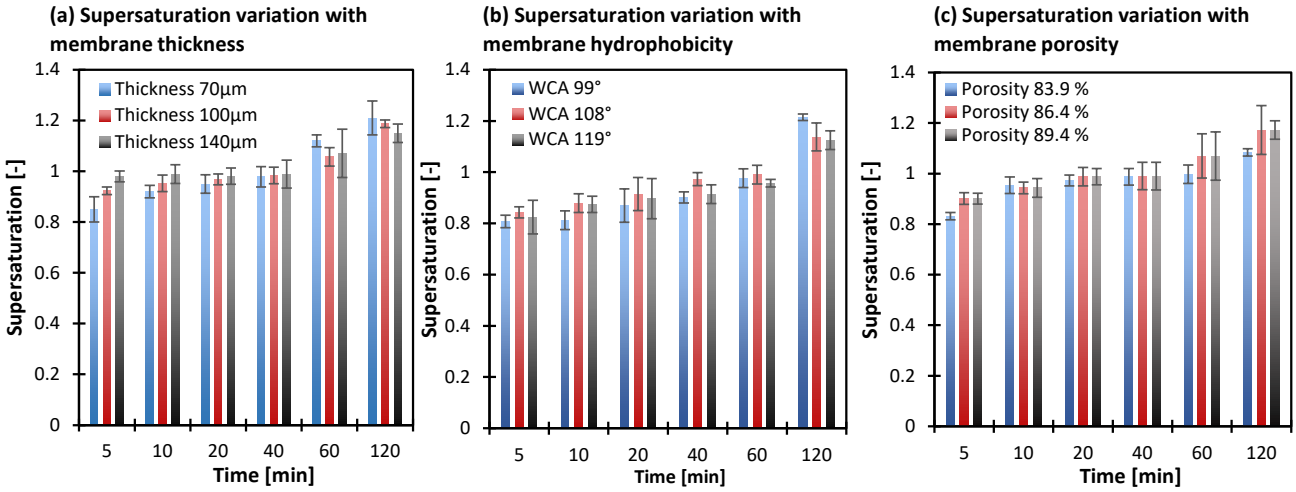

Fig. 7. Evolution of the supersaturation of the crystallization system with increase of ethanol concentration under the variation of membrane (a) thickness, (b) hydrophobicity and (c) porosity.

3.3.2. Crystal shape and size distribution

Glycine crystals had a prism-like shape with sizes in the range of 20-30 µm (Fig. 8). Depending on the membrane thickness, the mean crystal size slightly varied from 23, 24 and 26 µm for membrane thicknesses of 70, 100 and 140 µm respectively (Table S2). A higher antisolvent transmembrane flux increases the level of supersaturation, and favors nucleation, leading to smaller crystal size [67,68]. Crystals produced using membranes with water contact angle of 99, 108 and 119° showed average size of 31, 26 and 23 µm respectively. The antisolvent transmembrane flux is indeed highest for the most hydrophobic membrane (WCA of 119°), leading to higher supersaturation ratios (Fig. 7b) and an associated higher nucleation rate. This explains the narrower CSD and reduced crystal size (Fig. 8b). As for the impact of porosity (Fig. 8c), the resulting mean crystal size was 27, 24 and 24 µm using membrane porosities of 83.9, 86.4 and 89.4%, respectively. A higher porosity led to a higher mass transfer coefficient (Fig.6), but insignificant crystal size variation was observed. This is attributed to the direct correlation between the membrane porosity and hydrophobicity (Fig.3), as lower hydrophobicity facilitates nucleation as well, according to the classical nucleation theory [69], leading to smaller crystals.

Crystals recovered from the membrane surface had a broader CSD and a crystal size of c.a. 30 µm (Fig. S7) as opposed to 18-25 µm obtained from the bulk solution, which agrees with our previous findings using polypropylene (PP) membranes for MAAC crystallization of glycine [43]. Moreover, the size of the crystals produced on the surface of the membrane depends less on the membrane thickness contrary to the size of the crystals produced in the bulk solution, which can potentially be due to reduced hydrodynamics taking place at the vicinity of the membrane surface. At the membrane surface, less mixing occurs. The velocity of solution decreases from the bulk to the membrane surface given that the solution faces resistance from the surface [70]. Crystals at the membrane surface have more residence time allowing them to grow further. The XRD patterns (Fig. S9) correspond to a monoclinic system which characterizes α-glycine crystals, and agrees with the findings of Tuo *et al.* [38].

In this study, no change of crystal shape nor crystalline system was observed. Previously, an increase in operating temperature of both feed and antisolvent solutions partially softened the edges of the crystals [43], while it appeared in previous studies that MAAC can control as well the polymorphic nature [41]. It is then still open to investigation whether the membrane properties solely allow for crystal habit control. Nonetheless, this was previously achieved by varying the operating conditions, or feed conditions like concentration, using additives like polymer coating [40], or varying the solution pH [71].

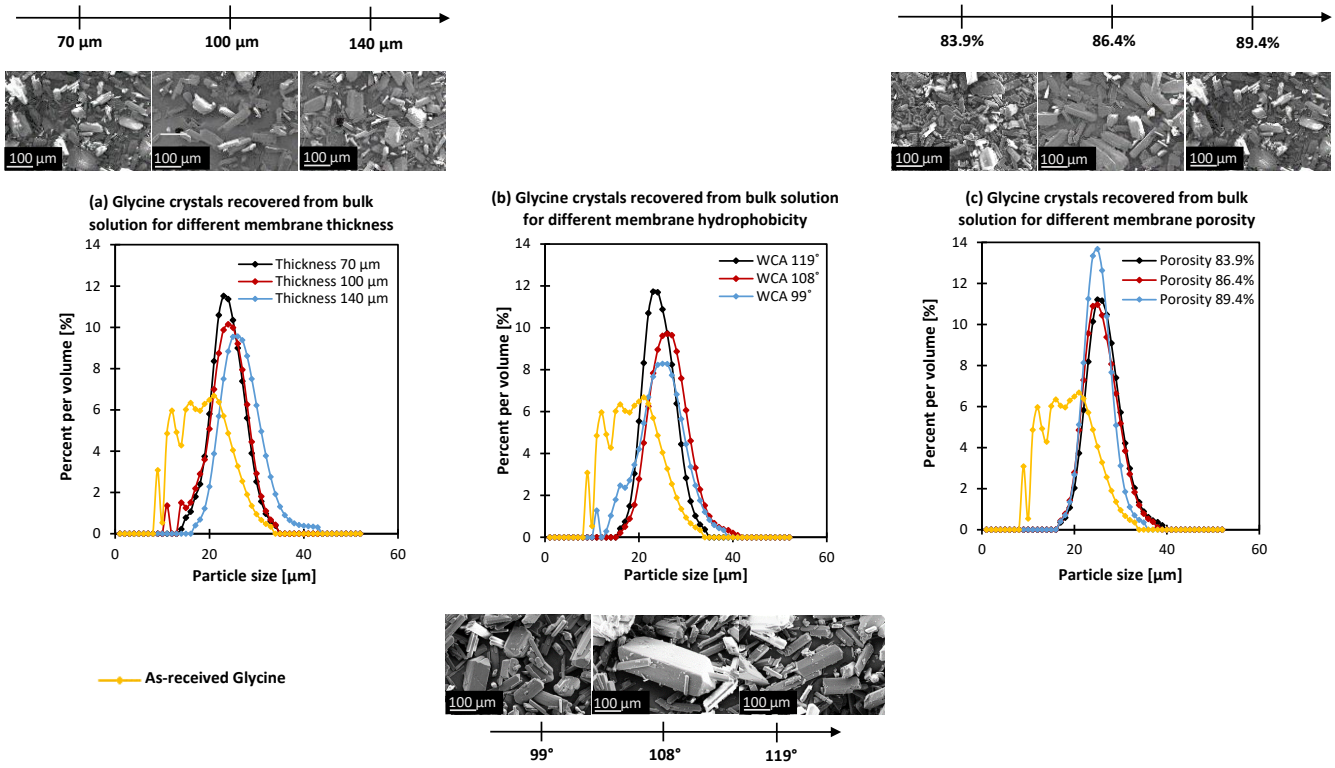

Fig. 8. Crystal morphology and size distribution recovered from bulk solution after 2-hour MAAC operation using membranes of different (a) thickness, (b) hydrophobicity and (c) porosity.

3.4. Possible membrane limitations for MAAC

3.4.1. Entrapment of crystals inside the membrane

The cross-section of the three membranes: one with 140 µm thickness, one with WCA of 119° and one with porosity 89.4% showed no traces of crystals formed along the membrane cross-section (Fig. 9). The presence of some entrapped organic compound was detected using TGA analysis (Fig. 10) with about 3% mass loss compared to the pristine membrane (darker curves). The absence of crystals at the membrane surface was also observed by Tuo *et al*. [38].

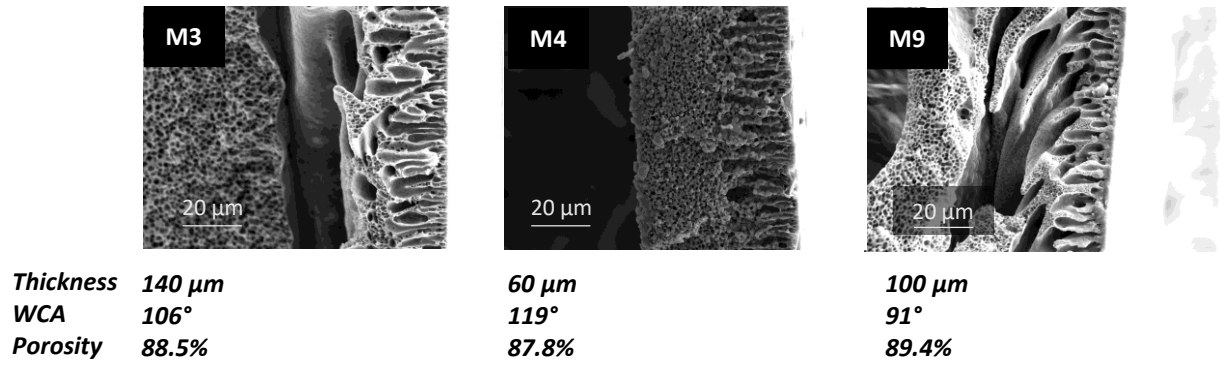

Fig. 9. Membranes cross sectional image after MAAC operation.

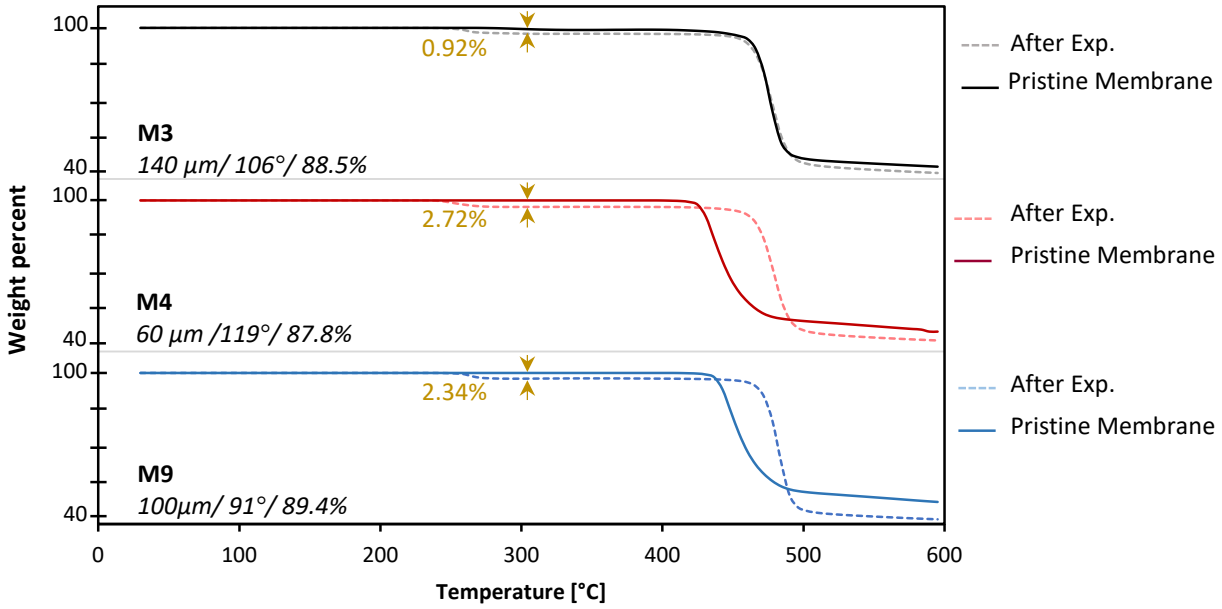

Fig. 10. TGA analysis of membranes after MAAC operation (dashed curves) to quantify the presence of crystals in the membranes. The dark curves correspond to the pristine membranes.

3.4.2. Membrane surface properties

The hydrophobicity slightly changes after MAAC operation (Fig. 11). Moreover, in FTIR spectra, a weak peak at 1615 cm^{-1} appeared when comparing the membranes before and after the experiment (Fig. 12), corresponding to a medium C=O stretching. This can once more be explained by a membrane contamination with some glycine. The presence of glycine in the membrane module can potentially be handled be handled by washing the membrane module with water at given intervals.

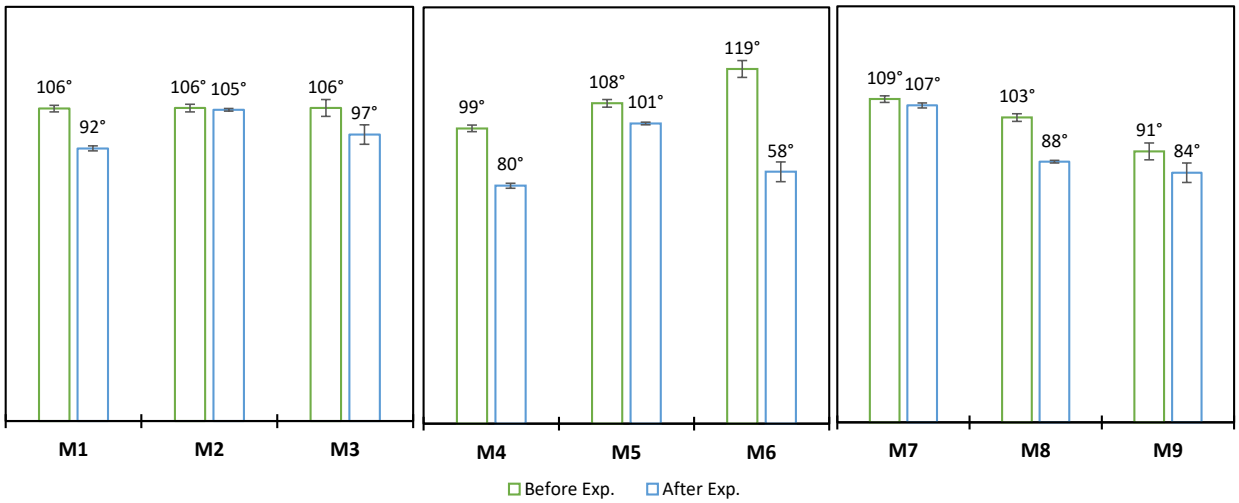

Fig. 11. Membrane hydrophobicity before and after MAAC experiments.

439

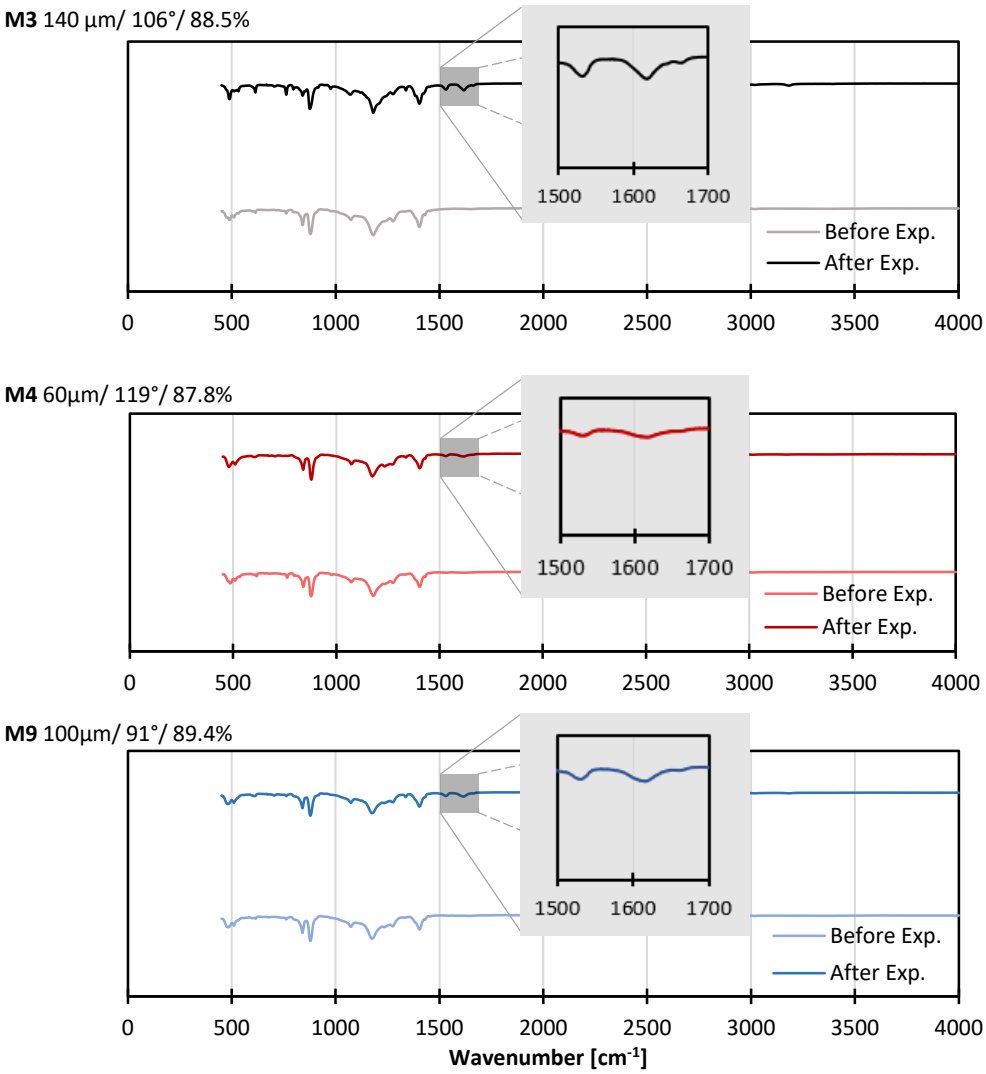

Fig. 12. FTIR spectra of membrane surfaces before and after MAAC operation. The membranes M_3, M_4 and M_9 gave both a narrow CSD and a stable mass transfer coefficient, so were chosen to have the optimum thickness, hydrophobicity, and porosity.

3.4.3. Membrane reusability

An optimum membrane was developed combining all characteristics that give the narrowest CSD and longer induction times (Fig. S10), i.e., a thickness of 140 µm, a WCA of 119° and 89.4% porosity. The same membrane was evaluated at three repetitions and the antisolvent was stable during the operation time (Fig. 13). All MAAC experiments were conducted at the same operating conditions, i.e., at 23°C temperature and 1 atm pressure, and maintaining the same velocities of the antisolvent and crystallizing solutions of 5 and 3.3 $\times 10^{-4}$ m/s respectively. All crystals possessed a prism-like shape and formed a narrow CSD (Fig. 14). The mean crystal size shifted with 4 µm in the second repetition, which could be due to variation in the surface characteristics.

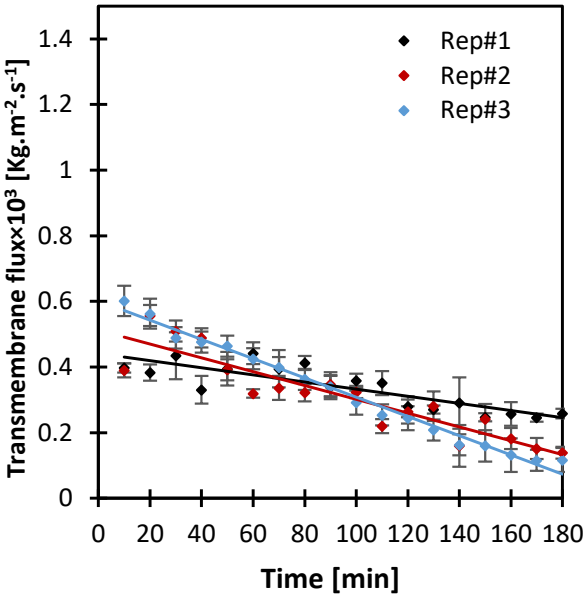

Fig. 13. Variation of antisolvent transmembrane flux with the repetitions using the same membrane of 140 µm thickness, 119° hydrophobicity and 89.4% porosity.

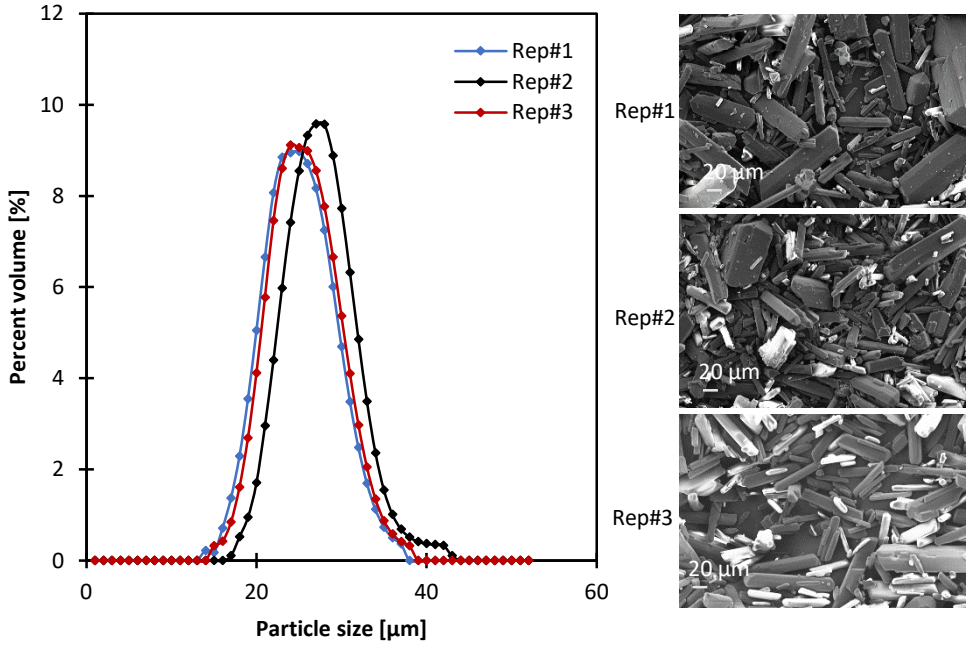

Fig. 14. Variation of antisolvent transmembrane flux with the repetitions using the same membrane of 140 µm thickness, 119° hydrophobicity and 89.4% porosity.

All membranes, regardless of their thickness, hydrophobicity or porosity successfully produced a narrow CSD without the need of additives or seeding, reducing the cost of raw material and the energy consumption. Hydrophobicity and thickness showed the most significant impact: the CSD got narrower when thickness decreases or hydrophobicity increases. Wu *et al.,* demonstrated that the mean size decreases and the CSD becomes narrower with increase of the mass ratio of the antisolvent to the solvent when using a jet crystallizer [24]. At the vicinity of the membrane surface, the antisolvent has its highest concentration as it permeates through the membrane pores, providing the conditions where the antisolvent concentration is higher than the solvent's, promoting a narrow crystal size distribution. Another phenomenon that is promoted at the same interface and contributes to the crystal size is the degree of mixing, such that every membrane pore represents an inlet to the antisolvent, preventing dead mixing zones [72].

The chemistry and morphology of surfaces often jointly determine the crystallization behavior. The presence of interfaces can modify the nucleation process either via favorable molecular interactions with the crystallizing molecule, or a lattice match between the substrate and the compound to be crystallized [22]. The traces of amino acid that were observed either through the TGA or FTIR analysis of the membrane could be a result of interactions between the substrate (the membrane) and the solute (glycine); nonetheless, it was not problematic for the reusability of the membrane as consistent crystal properties and transmembrane flux were obtained. For future comparative purposes, we recommend the provision of a detailed membrane description, and a consensual representation of the antisolvent mass transfer. The mass transfer coefficient is preferable in this case as it reflects solely the impact of the membrane characteristics on the antisolvent mass transfer [65]. Besides, crystallization kinetics differ from one system to another, so using a unified model crystallization system would also be key to constructing a clear assessment of any membrane in performing MAAC.

4. Conclusion

Membrane-assisted antisolvent crystallization (MAAC) is a new membrane technique to control crystallization from solution. The correlation between the membrane properties in defining the crystal characteristics of organic compounds was the subject of this study. PVDF porous membranes were synthesized of incremental thickness 70 to 140 um, hydrophobicity with WCA ranging from 99 to 119° and porosity from 83.9 to 89.4%. Glycine in ultrapure water was chosen as the model crystallization system, and ethanol as an antisolvent. All membranes were hydrophobic and had an asymmetric cross-sectional structure with a morphology based on a mix of finger- and sponge-like structures. The CSD of crystals had a narrow coefficient of variation (CV) in the range of 15 to 22%. This correlated directly with the antisolvent transmembrane mass transfer coefficient which was within the range of 0.4 and 1.6 $\times 10^{-4}$ $kg.m^{-2}.s^{-1}$ according to the different membrane characteristics. An optimum membrane was defined as a membrane which gave a stable antisolvent mass transfer and a narrow CSD while maintaining the prism shape of the glycine crystals. Accordingly, a final membrane with the thickness of 140 µm, WCA of 140° and a porosity of 89.4% was synthesized. This membrane gave a reproducible CSD, transmembrane antisolvent 0.4 to 0.6 $\times 10^{-3}$ $kg.m^{-2}.s^{-1}$ and an 80-minute longer induction time. This study contributes to understanding the key membrane characteristics in controlling antisolvent crystallization.

Appendices

Table A1 Overview of studies osn membrane-assisted antisolvent crystallization where the concentration/ activity difference is used as driving force. *[A] and [CS] stand for the antisolvent and the crystallizing solution respectively.

Crystallization system*	Membrane characteristics				Antisolvent mass transfer		Crystal properties		Ref.
	Hydrophobicity (WCA)	Thickness [µm]	Porosity [%]	Other	Flux/ flow rate	Mass transfer coefficient	Crystal size	Crystal size distribution (CV)	
[A] Ethanol; [CS] L-serine in water	120-150	-	-	• Pore size: 0.2 µm; • Membrane material PVDF and PP.	0.0002 – 0.003 $Kg/m^2.s$	0.0023-0.0048 $kg/m^2.s$	89-102 µm.	31-37 %	[35]
[A] 2-Propanol; [CS] L-asparagine in de-ionized water.	-	-	40	• Tortuosity: 2.4; • Pore size: 0.03 µm; • Membrane material: PP.	100 to 500 $\mu m.s^{-1}$	-	70 µm	-	[37]
[A] Ethanol; [CS] A solution of erythritol and ultrapure water.	83	319	58	• Tortuosity: 4.45; • Membrane material: PES.	2 - 4 $kg.m^{-2}.h^{-1}$	-	<20 µm	48%	[38]
[A] Deionized water; [CS] Indomethacin in ethanol.	-	-	-	• Pore size: 0.10, 0.25 and 0.45 µm; • Membrane material: Polyethylene.	1.2 – 1.4 m/s	-	0.3 to 0.35 µm	-	[39]
[A] Deionized water; [CS] Drug particles of Griseofulvin in acetone.	-	200	75	• Pore size: 0.2 µm; • Membrane material: hydrophilic Nylon-6.	-	-	1.6 – 11.7 µm	-	[40]
[A] Water and ethanol mixture with different compositions at 30 °C; [CS] Glycine solution in bi-distilled water at 10 °C.	-	-	-	• Pore size: 0.22 µm; • Membrane material: PP.	1.53 or 9.1×10^{-4} Lh^{-1}	-	-	-	[41]
[A] Ethanol; [CS] A solution of NaCl and ultrapure water	108	319	53	Membrane material: PTFE.	-	-	41.6 µm.	43.5%	[44]
[A] Ethanol; [CS] Glycine in water.	150	-	-	• Membrane material: PP.	0.2–1 $\times 10^{-2}$ $kg/m^2.s$	-	23–40 µm	50–60%	[43]

[A] Ethanol; [CS] Erythritol in water.	83	320	58	• Pore size: 0.03 µm; • Tortuosity: 1.45; • Membrane material: PES.	1.2 – 2.8 $kg.m^{-2}.h^{-1}$	-	50 µm	50.9%	[73]

Acknowledgements

This study falls under the project PURE- 20/25-108 – "New approaches in Process Intensification: Towards combined PUrefication-REaction Membrane based processes," from Actions de Recherche Concertées funded by Wallonia-Bruxelles Federation in Belgium.

References

[1] J. Wang, F. Li, R. Lakerveld, Process intensification for pharmaceutical crystallization, Chem. Eng. Process. - Process Intensif. 127 (2018) 111–126. https://doi.org/10.1016/j.cep.2018.03.018.

[2] N. Yazdanpanah, Z.K. Nagy, eds., The handbook of continuous crystallization, Royal Society of Chemistry, London, 2020.

[3] H. Julian, S. Meng, H. Li, Y. Ye, V. Chen, Effect of operation parameters on the mass transfer and fouling in submerged vacuum membrane distillation crystallization (VMDC) for inland brine water treatment, J. Membr. Sci. 520 (2016) 679–692. https://doi.org/10.1016/j.memsci.2016.08.032.

[4] W. Lin, Y. Zhang, D. Li, X. Wang, X. Huang, Roles and performance enhancement of feed spacer in spiral wound membrane modules for water treatment: A 20-year review on research evolvement, Water Res. 198 (2021) 117146. https://doi.org/10.1016/j.watres.2021.117146.

[5] C. Stoquart, P. Servais, P.R. Bérubé, B. Barbeau, Hybrid Membrane Processes using activated carbon treatment for drinking water: A review, J. Membr. Sci. 411–412 (2012) 1–12. https://doi.org/10.1016/j.memsci.2012.04.012.

[6] Y. Shi, J. Huang, G. Zeng, W. Cheng, J. Hu, Photocatalytic membrane in water purification: is it stepping closer to be driven by visible light?, J. Membr. Sci. 584 (2019) 364–392. https://doi.org/10.1016/j.memsci.2019.04.078.

[7] A. El Fadil, R. Verbeke, M. Kyburz, P. E.M. Aerts, IvoF.J. Vankelecom, From academia to industry: Success criteria for upscaling nanofiltration membranes for water and solvent applications, J. Membr. Sci. (2023) 121393. https://doi.org/10.1016/j.memsci.2023.121393.

[8] D.F. Stamatialis, B.J. Papenburg, M. Gironés, S. Saiful, S.N.M. Bettahalli, S. Schmitmeier, M. Wessling, Medical applications of membranes: Drug delivery, artificial organs and tissue engineering, J. Membr. Sci. 308 (2008) 1–34. https://doi.org/10.1016/j.memsci.2007.09.059.

[9] E. Yi, H.S. Kang, S.M. Lim, H.J. Heo, D. Han, J.F. Kim, A. Park, D.H. Choi, Y.-I. Park, H. Park, Y.H. Cho, E.-H. Sohn, Superamphiphobic blood-repellent surface modification of porous fluoropolymer membranes for blood oxygenation applications, J. Membr. Sci. 648 (2022) 120363. https://doi.org/10.1016/j.memsci.2022.120363.

[10] S. Bavarella, A. Brookes, A. Moore, P. Vale, G. Di Profio, E. Curcio, P. Hart, M. Pidou, E.J. McAdam, Chemically reactive membrane crystallisation reactor for CO2–NH3 absorption and ammonium bicarbonate crystallisation: Kinetics of heterogeneous crystal growth, J. Membr. Sci. 599 (2020) 117682. https://doi.org/10.1016/j.memsci.2019.117682.

[11] T. Chen, Y. Xu, Y. Zhang, Y. Gong, Y. Zhang, J.Y.S. Lin, Double-layer ceramic-carbonate hollow fiber membrane with superior mechanical strength for CO2 separation, J. Membr. Sci. 658 (2022) 120701. https://doi.org/10.1016/j.memsci.2022.120701.

[12] L. Wang, S. Fan, X. Li, M.O. Tadé, S. Liu, Rational Design of Carbon-Based Porous Aerogels with Nitrogen Defects and Dedicated Interfacial Structures toward Highly Efficient CO_2 Greenhouse Gas Capture and Separation, ACS Omega. 7 (2022) 40184–40194. https://doi.org/10.1021/acsomega.2c05072.
[13] V. Sang Sefidi, P. Luis, Advanced Amino Acid-Based Technologies for CO_2 Capture: A Review, Ind. Eng. Chem. Res. 58 (2019) 20181–20194. https://doi.org/10.1021/acs.iecr.9b01793.
[14] C.A. Quist-Jensen, A. Ali, S. Mondal, F. Macedonio, E. Drioli, A study of membrane distillation and crystallization for lithium recovery from high-concentrated aqueous solutions, J. Membr. Sci. 505 (2016) 167–173. https://doi.org/10.1016/j.memsci.2016.01.033.
[15] S. Meng, Y. Ye, J. Mansouri, V. Chen, Crystallization behavior of salts during membrane distillation with hydrophobic and superhydrophobic capillary membranes, J. Membr. Sci. 473 (2015) 165–176. https://doi.org/10.1016/j.memsci.2014.09.024.
[16] M.-C. Sparenberg, B. Hanot, C. Molina-Fernández, P. Luis, Experimental mass transfer comparison between vacuum and direct contact membrane distillation for the concentration of carbonate solutions, Sep. Purif. Technol. 275 (2021) 119193. https://doi.org/10.1016/j.seppur.2021.119193.
[17] M.-C. Sparenberg, S. Chergaoui, V. Sang Sefidi, P. Luis, Crystallization control via membrane distillation-crystallization: A review, Desalination. 519 (2021) 115315. https://doi.org/10.1016/j.desal.2021.115315.
[18] E. Chabanon, D. Mangin, C. Charcosset, Membranes and crystallization processes: State of the art and prospects, J. Membr. Sci. 509 (2016) 57–67. https://doi.org/10.1016/j.memsci.2016.02.051.
[19] P. Das, S. Dutta, K.K. Singh, Insights into membrane crystallization: A sustainable tool for value added product recovery from effluent streams, Sep. Purif. Technol. 257 (2021) 117666. https://doi.org/10.1016/j.seppur.2020.117666.
[20] J. Capdevila-Echeverria, J. Wang, R. Lakerveld, J.H. ter Horst, Process modeling and optimization of continuous chiral resolution by integration of membrane and crystallization technologies, J. Membr. Sci. 632 (2021) 119359. https://doi.org/10.1016/j.memsci.2021.119359.
[21] H. Takiyama, Anti-solvent Crystallization Method for Production of Desired Crystalline Particles, in: M. Sakamoto, H. Uekusa (Eds.), Adv. Org. Cryst. Chem., Springer Singapore, Singapore, 2020: pp. 53–70. https://doi.org/10.1007/978-981-15-5085-0_3.
[22] K. Harano, T. Homma, Y. Niimi, M. Koshino, K. Suenaga, L. Leibler, E. Nakamura, Heterogeneous nucleation of organic crystals mediated by single-molecule templates, Nat. Mater. 11 (2012) 877–881. https://doi.org/10.1038/nmat3408.
[23] F. Ito, Y. Suzuki, J. Fujimori, T. Sagawa, M. Hara, T. Seki, R. Yasukuni, M.L. de la Chapelle, Direct Visualization of the Two-step Nucleation Model by Fluorescence Color Changes during Evaporative Crystallization from Solution, Sci. Rep. 6 (2016) 22918. https://doi.org/10.1038/srep22918.
[24] B. Wu, J. Li, C. Li, J. He, P. Luo, Antisolvent crystallization intensified by a jet crystallizer and a method for investigating crystallization kinetics, Chem. Eng. Sci. 211 (2020) 115259. https://doi.org/10.1016/j.ces.2019.115259.
[25] A.J. Alvarez, A.S. Myerson, Continuous Plug Flow Crystallization of Pharmaceutical Compounds, Cryst. Growth Des. 10 (2010) 2219–2228. https://doi.org/10.1021/cg901496s.
[26] S. Pal, K. Madane, A.A. Kulkarni, Antisolvent based precipitation: Batch, capillary flow reactor and impinging jet reactor, Chem. Eng. J. 369 (2019) 1161–1171. https://doi.org/10.1016/j.cej.2019.03.107.
[27] T. Tari, Z. Fekete, P. Szabó-Révész, Z. Aigner, Reduction of glycine particle size by impinging jet crystallization, Int. J. Pharm. 478 (2015) 96–102. https://doi.org/10.1016/j.ijpharm.2014.11.021.
[28] S. Pal, K. Madane, M. Mane, A.A. Kulkarni, Impingement Dynamics of Jets in a Confined Impinging Jet Reactor, Ind. Eng. Chem. Res. 60 (2021) 969–979. https://doi.org/10.1021/acs.iecr.0c04717.
[29] J. Cottet, P. Renaud, Introduction to microfluidics, in: Drug Deliv. Devices Ther. Syst., Elsevier, 2021: pp. 3–17. https://doi.org/10.1016/B978-0-12-819838-4.00014-6.

[30] M.S. Emami, M. Haghshenasfard, R. Zarghami, R. Sadeghi, M.N. Esfahany, CFD simulation and experimental study of antisolvent precipitation through impinging jets for synthesis of nanodrug particles, J. Mol. Liq. 367 (2022) 120348. https://doi.org/10.1016/j.molliq.2022.120348.
[31] M.N. Hussain, J. Jordens, J.J. John, L. Braeken, T. Van Gerven, Enhancing pharmaceutical crystallization in a flow crystallizer with ultrasound: Anti-solvent crystallization, Ultrason. Sonochem. 59 (2019) 104743. https://doi.org/10.1016/j.ultsonch.2019.104743.
[32] K. Madane, V.V. Ranade, Anti-solvent crystallization: Particle size distribution with different devices, Chem. Eng. J. 446 (2022) 137235. https://doi.org/10.1016/j.cej.2022.137235.
[33] E.M. Peters, M. Svärd, K. Forsberg, Impact of process parameters on product size and morphology in hydrometallurgical antisolvent crystallization, CrystEngComm. 24 (2022) 2851–2866. https://doi.org/10.1039/D2CE00050D.
[34] E. Curcio, S. Simone, G.D. Profio, E. Drioli, A. Cassetta, D. Lamba, Membrane crystallization of lysozyme under forced solution flow, J. Membr. Sci. 257 (2005) 134–143. https://doi.org/10.1016/j.memsci.2004.07.037.
[35] S. Chergaoui, D.P. Debecker, T. Leyssens, P. Luis, Control of Antisolvent Mass Transfer through Porous Membranes for the Crystallization of Organic Compounds, Cryst. Growth Des. (2023). https://doi.org/10.1021/acs.cgd.3c00408.
[36] D. Chen, B. Wang, K.K. Sirkar, Hydrodynamic modeling of porous hollow fiber anti-solvent crystallizer for continuous production of drug crystals, J. Membr. Sci. 556 (2018) 185–195. https://doi.org/10.1016/j.memsci.2018.03.046.
[37] D.M. Zarkadas, K.K. Sirkar, Antisolvent crystallization in porous hollow fiber devices, Chem. Eng. Sci. 61 (2006) 5030–5048. https://doi.org/10.1016/j.ces.2006.03.036.
[38] L. Tuo, X. Ruan, W. Xiao, X. Li, G. He, X. Jiang, A novel hollow fiber membrane-assisted antisolvent crystallization for enhanced mass transfer process control, AIChE J. 65 (2019) 734–744. https://doi.org/10.1002/aic.16438.
[39] J.C.W. Fern, S. Ohsaki, S. Watano, R. Pfeffer, Continuous synthesis of nano-drug particles by antisolvent crystallization using a porous hollow-fiber membrane module, Int. J. Pharm. 543 (2018) 139–150. https://doi.org/10.1016/j.ijpharm.2018.03.025.
[40] D. Chen, D. Singh, K.K. Sirkar, R. Pfeffer, Continuous Synthesis of Polymer-Coated Drug Particles by Porous Hollow Fiber Membrane-Based Antisolvent Crystallization, Langmuir. 31 (2015) 432–441. https://doi.org/10.1021/la503179t.
[41] G. Di Profio, C. Stabile, A. Caridi, E. Curcio, E. Drioli, Antisolvent membrane crystallization of pharmaceutical compounds, J. Pharm. Sci. 98 (2009) 4902–4913. https://doi.org/10.1002/jps.21785.
[42] G.D. Profio, A. Caridi, R. Caliandro, A. Guagliardi, E. Curcio, E. Drioli, Fine Dosage of Antisolvent in the Crystallization of L -Histidine: Effect on Polymorphism, Cryst. Growth Des. 10 (2010) 449–455. https://doi.org/10.1021/cg901038g.
[43] S. Chergaoui, D.P. Debecker, T. Leyssens, P. Luis, Key Parameters Impacting the Crystal Formation in Antisolvent Membrane-Assisted Crystallization, Membranes. 13 (2023) 140. https://doi.org/10.3390/membranes13020140.
[44] L. Sheng, J. Li, G. He, W. Xiao, X. Yan, X. Li, X. Ruan, X. Jiang, Visual study and simulation of interfacial liquid layer mass transfer in membrane-assisted antisolvent crystallization, Chem. Eng. Sci. 228 (2020) 116003. https://doi.org/10.1016/j.ces.2020.116003.
[45] G. Di Profio, V. Grosso, A. Caridi, R. Caliandro, A. Guagliardi, G. Chita, E. Curcio, E. Drioli, Direct production of carbamazepine–saccharin cocrystals from water/ethanol solvent mixtures by membrane-based crystallization technology, CrystEngComm. 13 (2011) 5670. https://doi.org/10.1039/c1ce05410d.
[46] A. Caridi, G. Di Profio, R. Caliandro, A. Guagliardi, E. Curcio, E. Drioli, Selecting the Desired Solid Form by Membrane Crystallizers: Crystals or Cocrystals, Cryst. Growth Des. 12 (2012) 4349–4356. https://doi.org/10.1021/cg300702t.
[47] F. Liu, N.A. Hashim, Y. Liu, M.R.M. Abed, K. Li, Progress in the production and modification of PVDF membranes, J. Membr. Sci. 375 (2011) 1–27. https://doi.org/10.1016/j.memsci.2011.03.014.

[48] M.M. Aji, S. Narendren, M.K. Purkait, V. Katiyar, Utilization of waste polyvinyl chloride (PVC) for ultrafiltration membrane fabrication and its characterization, J. Environ. Chem. Eng. 8 (2020) 103650. https://doi.org/10.1016/j.jece.2019.103650.
[49] A. Mersmann, ed., Crystallization technology handbook, 2nd ed., rev.expanded, Marcel Dekker, New York, 2001.
[50] Z. Cui, X. Li, Y. Zhang, Z. Wang, A. Gugliuzza, F. Militano, E. Drioli, F. Macedonio, Testing of three different PVDF membranes in membrane assisted-crystallization process: Influence of membrane structural-properties on process performance, Desalination. 440 (2018) 68–77. https://doi.org/10.1016/j.desal.2017.12.038.
[51] S. Capizzano, M. Frappa, E. Drioli, F. Alessandro, F. Macedonio, Chemical interaction between PVDF and Li cations during LiCl crystallization in VMCr, J. Membr. Sci. 658 (2022) 120733. https://doi.org/10.1016/j.memsci.2022.120733.
[52] S. Nejati, C. Boo, C.O. Osuji, M. Elimelech, Engineering flat sheet microporous PVDF films for membrane distillation, J. Membr. Sci. 492 (2015) 355–363. https://doi.org/10.1016/j.memsci.2015.05.033.
[53] S. Mazinani, S. Darvishmanesh, A. Ehsanzadeh, B. Van der Bruggen, Phase separation analysis of Extem/solvent/non-solvent systems and relation with membrane morphology, J. Membr. Sci. 526 (2017) 301–314. https://doi.org/10.1016/j.memsci.2016.12.031.
[54] Q. Zhang, S. Zhang, Y. Zhang, X. Hu, Y. Chen, Preparation of PVDF/PVC composite membrane for wastewater purification, Desalination Water Treat. 51 (2013) 3854–3857. https://doi.org/10.1080/19443994.2013.781735.
[55] A. Karimi, A. Khataee, V. Vatanpour, M. Safarpour, The effect of different solvents on the morphology and performance of the ZIF-8 modified PVDF ultrafiltration membranes, Sep. Purif. Technol. 253 (2020) 117548. https://doi.org/10.1016/j.seppur.2020.117548.
[56] S. Devi, P. Ray, K. Singh, P.S. Singh, Preparation and characterization of highly micro-porous PVDF membranes for desalination of saline water through vacuum membrane distillation, Desalination. 346 (2014) 9–18. https://doi.org/10.1016/j.desal.2014.05.004.
[57] P.M. Esfarjani, H. Fashandi, M. Karevan, A. Moheb, Tuning poly(vinyl chloride) membrane morphology to suit vacuum membrane distillation: Focusing on membrane preparation process based on phase separation, Colloids Surf. Physicochem. Eng. Asp. 630 (2021) 127610. https://doi.org/10.1016/j.colsurfa.2021.127610.
[58] M.L. Yeow, Y.T. Liu, K. Li, Morphological study of poly(vinylidene fluoride) asymmetric membranes: Effects of the solvent, additive, and dope temperature, J. Appl. Polym. Sci. 92 (2004) 1782–1789. https://doi.org/10.1002/app.20141.
[59] M.L. Yeow, Y.T. Liu, K. Li, Isothermal phase diagrams and phase-inversion behavior of poly(vinylidene fluoride)/solvents/additives/water systems, J. Appl. Polym. Sci. 90 (2003) 2150–2155. https://doi.org/10.1002/app.12846.
[60] J. Wang, L. Zheng, Z. Wu, Y. Zhang, X. Zhang, Fabrication of hydrophobic flat sheet and hollow fiber membranes from PVDF and PVDF-CTFE for membrane distillation, J. Membr. Sci. 497 (2016) 183–193. https://doi.org/10.1016/j.memsci.2015.09.024.
[61] Y. Diao, T. Harada, A.S. Myerson, T. Alan Hatton, B.L. Trout, The role of nanopore shape in surface-induced crystallization, Nat. Mater. 10 (2011) 867–871. https://doi.org/10.1038/nmat3117.
[62] E. Curcio, V. Curcio, G.D. Profio, E. Fontananova, E. Drioli, Energetics of Protein Nucleation on Rough Polymeric Surfaces, J. Phys. Chem. B. 114 (2010) 13650–13655. https://doi.org/10.1021/jp106349d.
[63] X. Chen, J.A. Weibel, S.V. Garimella, Water and Ethanol Droplet Wetting Transition during Evaporation on Omniphobic Surfaces, Sci. Rep. 5 (2015) 17110. https://doi.org/10.1038/srep17110.
[64] R. Shukla, M. Cheryan, Performance of ultrafiltration membranes in ethanol–water solutions: effect of membrane conditioning, J. Membr. Sci. 198 (2002) 75–85. https://doi.org/10.1016/S0376-7388(01)00638-X.
[65] P. Luis, ed., Fundamental Modeling of Membrane Systems: Membrane and Process Performance, 1st edition, Elsevier, Cambridge, MA, 2018.

[66] D. Du, Novel, Calibration-Free Strategies for Supersaturation Control in Antisolvent Crystallization Processes, Cryst Growth Des. (2013) 12.
[67] Z. Gao, S. Rohani, J. Gong, J. Wang, Recent Developments in the Crystallization Process: Toward the Pharmaceutical Industry, Engineering. 3 (2017) 343–353. https://doi.org/10.1016/J.ENG.2017.03.022.
[68] S.M. D'Addio, R.K. Prud'homme, Controlling drug nanoparticle formation by rapid precipitation, Adv. Drug Deliv. Rev. 63 (2011) 417–426. https://doi.org/10.1016/j.addr.2011.04.005.
[69] E. Drioli, G. Di Profio, E. Curcio, Membrane-Assisted Crystallization Technology, IMPERIAL COLLEGE PRESS, 2015. https://doi.org/10.1142/p912.
[70] C.M. Romero, G.P. Trujillo, L.M.P. Verissimo, M.A. Esteso, M.L. Ramos, A.C.F. Ribeiro, Limiting diffusion coefficients of α,ω-amino acids in water and in sodium chloride aqueous solutions at 298.15 K, Eur. Phys. J. E. 42 (2019) 94. https://doi.org/10.1140/epje/i2019-11856-1.
[71] J.-C. Hsueh, K.L. Yeh, H.L. Lee, T. Lee, Strategy for polymorphic control by enzymatic reaction and antisolvent crystallization: effect of aminoacylase on metastable β-glycine formation, React. Chem. Eng. 6 (2021) 2292–2305. https://doi.org/10.1039/D1RE00335F.
[72] Crystallization: Basic Concepts and Industrial Applications | Wiley, Wiley.Com. (n.d.). https://www.wiley.com/en-us/Crystallization%3A+Basic+Concepts+and+Industrial+Applications-p-9783527327621 (accessed March 30, 2021).
[73] J. Li, L. Sheng, L. Tuo, W. Xiao, X. Ruan, X. Yan, G. He, X. Jiang, Membrane-Assisted Antisolvent Crystallization: Interfacial Mass-Transfer Simulation and Multistage Process Control, Ind. Eng. Chem. Res. 59 (2020) 10160–10171. https://doi.org/10.1021/acs.iecr.0c01645.